IEEE Access
Multidisciplinary ⋮ Rapid Review ⋮ Open Access Journal

Received September 23, 2021, accepted October 13, 2021, date of publication October 19, 2021, date of current version October 27, 2021.

Digital Object Identifier 10.1109/ACCESS.2021.3121341

The Influence of Metastable Species and Rotational Quantum Numbers on the Derivation of OH (A–X), NO-γ (A–X) and N_2 (C–B) Bands Rotational Temperatures in an Argon Gas-Liquid-Phase Plasma Discharge

HAFIZ IMRAN AHMAD QAZI AND JIAN-JUN HUANG

SZU-CASIPP Joint Laboratory for Applied Plasma, College of Physics and Optoelectronic Engineering, Shenzhen University, Shenzhen 518060, China

Corresponding author: Jian-Jun Huang (huangjj@szu.edu.cn)

This work was supported by the National MCF Energy Research and Development Program under Grant 2019YFE03130002.

ABSTRACT In this work, the rotational temperatures of the atmospheric pressure AC-excited argon gas-liquid-phase discharge estimated by employing disparate spectroscopic methods on the rotational structure of molecular OH (A–X), NO-γ (A–X), and N_2 (C–B) bands-spectra emanating from the gas-phase discharge region were compared with those obtained from the liquid-phase region to analyze their variations based on the metastable species and rotational quantum numbers. The electrical characteristics and images of the discharge were also examined to analyze the discharge nature. Realization of the estimated values for rotational temperatures, as an estimation of the gas temperature, depend on thermalization of the accounted excited rotational population levels. Excitations to higher rotational quantum numbers (N') inhibited thermalization of the rotational distributions, and the rotational temperatures were found to increase proportionally with excitations to higher N' numbers. The phenomenon of rotational excitation to higher N' numbers was particularly prominent for the wet discharge region, and thus, substantially higher rotational temperatures were obtained. The excitation to higher N' numbers is related to the basic production processes largely those involving Ar^*_{meta} and N_2 (A) metastable states that populate predominantly the levels with large N' numbers (e.g., $N' = 8$ and $N' = 25$, respectively for OH and NO), and thus, their contemplated rotational population is not indicative of the kinetic gas temperature. With respect to spectral diagnostics techniques, the Boltzmann plot constructed by adopting a unique single fitting model (compared to the conventional double fitting models approach used for liquid discharges) only calculating the rotational population of the Q_1 branch of OH (A–X) for lower N' numbers ($N' \leq 4$) affords the opportunity to estimate the gas temperature in wet plasma discharge.

INDEX TERMS Argon gas-liquid-phase discharge, molecular emission spectra, rotational population distribution, production processes, rotational temperature.

I. INTRODUCTION

Over the last several decades, non-equilibrium discharges on and within liquid surfaces have rapidly evolved because of their great impact in diverse fields such as cancer treatment, lithotripsy, plant growth enhancement, water decontamination, chemical analysis of complex mixtures, and nanoparticle synthesis [1]–[9]. In comparison to conventional atmospheric pressure glow discharges excited between metallic electrodes, the chemistry and physics related to plasma discharges in liquids electrodes are somewhat less well understood. This is because these discharges are typically excited in both the gas- and liquid-phases, and are relatively chaotic in nature [10]. Moreover, in the discharge assembly where the liquid typically serves as one of the electrodes, it is found that the electrodes tend not only to evaporate but also undergo deformation. These factors add significant complexity to the experimental configuration, and the associated discharge

The associate editor coordinating the review of this manuscript and approving it for publication was Muhammad Imran Tariq.

This work is licensed under a Creative Commons Attribution 4.0 License. For more information, see https://creativecommons.org/licenses/by/4.0/

processes become fairly intricate when compared with the non-thermal gas-phase discharges (plasmas) between metallic electrodes.

Investigations conducted to evaluate the non-equilibrium plasmas on and within liquid surfaces have revealed a broad range of methodologies, applications, and phenomena whereby a large number of articles have addressed this specific topic [8], [11]. The advances in plasma diagnostics necessarily comes up against the need to characterize comprehensively the fundamental processes occurring in such plasmas and also to develop and apply adequate models which can substantiate the characterization techniques. In this regard, optical emission spectroscopy has long been accepted as a valuable technique for characterizing and exploring the basic physical parameters of plasmas and is frequently applied to predict the rotational temperature (T_{rot}) of plasmas based on measurement of the excited rotational population distributions of various diatomic molecules such as OH (A–X), NO-γ (A–X), and N_2 (C–B). Therefore, it is important to have an in-depth understanding of this particular characterization technique, especially for the case of atmospheric pressure non-equilibrium plasmas generated in a gas-liquid environment or in a complex mixture comprising various molecular species. It is often not the case that the densities of the considered excited rotational states for the case of the diatomic molecules (in non-equilibrium plasmas) are in thermal equilibrium with the translational temperature (gas temperature, T_{gas}) [12]. Non-Boltzmann distributions which are witnessed in the rotational spectra of non-equilibrium plasmas obviously demonstrate the significance of being able to inspect carefully the rotational structure of the spectra.

As for conventionally applied methodologies, in many cases, the T_{rot} of non-equilibrium plasmas has often been predicted from the emission band of OH (A–X) [13]. In the case of a discharge operating in humid conditions, the population of higher rotational quantum numbers (N') is substantially overpopulated, and shows a clear deviation from the Boltzmann law. It is accepted that this overpopulation is less dominant for lower N' numbers. Thus, in the Boltzmann plot method, a two-temperature fitting methodology is typically adopted to characterize the population of rotational levels. And the T_{rot} of OH (A–X) comes from the slope of the linear fit corresponding to the populations with low N' numbers. One of the major disadvantages of this technique is that it is necessary to access highly resolved spectra to construct the plot for the whole range of N' numbers along with the corresponding populations. Thus, as an alternative, a calculation using LIFBASE software calculation has also been used in numerous investigations to derive the T_{rot} from poorly resolved rotational structure of OH (A–X) [14]–[17]. This software has also been employed for other molecular bands to calculate the T_{rot}. For example, it was used to derive the T_{rot} from the gamma-band system of NO [NO-γ (A–X)] [16]. Besides, in other works, as an alternative to OH (A–X) and NO-γ (A–X), the nitrogen second positive system [SPS N_2 (C–B)] bands were calculated with SPECAIR software to approximate the T_{rot} [18]–[20]. The latter are convenient for calculating the partially resolved emission spectra; however, their main drawback is that an assumption is made that the obtained shape of the populated rotational distribution is Boltzmann/non-Boltzmann. Irrespective of such a drawback, the former techniques have been applied successfully to measure the T_{rot} in many plasma discharges. Nonetheless, their utilization for OH (A–X), NO-γ (A–X), and SPS N_2 (C–B) diatomic molecular emission transition bands have resulted in discrepancies among the derived T_{rot}, especially in respect of discharges on and within liquids.

In an atmospheric pressure vapor bubble plasma discharge, for instance, a non-Boltzmann distribution was demonstrated for the OH (A–X) rotational structure, in which rotational states with rotational numbers $N' > 10$ were overpopulated, and the yielded T_{rot} of 8800 K was much higher than the T_{gas} of 1550 K as derived from the T_{rot} of N_2 (C) [20]. This clearly means that a non-Boltzmann rotational distribution is characterized by the production mechanism that leads to an efficient excitation of OH (A) to higher N' numbers. A non-equilibrium distribution of OH (A–X) has also been found and investigated in other studies [11], and discrepancies were reported among the predicted T_{rot} of OH (A–X) and N_2 (C–B) at atmospheric pressure. In an argon gas-liquid-phase discharge, the OH (A–X) band rotational population adaptation in a Boltzmann plot resulted in a T_{rot} value which was comparatively higher than the T_{gas}, and this was ascribed to the fact that the production process was boosted as a consequence of diffusion of water content in the discharge region [21]. Non-Boltzmann behavior is not only realized for OH (A–X) band rotational distribution; for example, highly populated higher rotational levels were also observed for N_2 (C) in a N_2O bubble discharge in water [12]. The T_{rot} of N_2 (C) was found to be higher than for cases in which the plasma was filled with air and N_2. The high value of T_{rot} was associated with N_2 (C) excitation through the processes such as dissociative electron recombination of N_2O^+ and dissociative electron excitation of N_2O that result in rotational excitation to higher N' numbers in a N_2O discharge. Apart from these, the emission spectra have been studied for the presence of diatomic molecules such as N_2, NO, OH, etc., which were measured in an open-air discharge with electrodes based on the use of tap water [22]. The predicted T_{rot} values obtained from OH (A–X), and particularly, NO-γ (A–X), exceeded substantially the estimated T_{rot} of N_2 (C–B), and consequently the T_{gas}. The difference in the calculated T_{rot} was associated with the impact of the production mechanisms, as well as with the decay of the excited states.

The common trend identified in the characterization studies on such plasma discharges initiated on and within liquid surfaces is the utilization of spectroscopic diagnostics to predict the T_{rot}. Additionally, investigations seek to introduce improvements, especially in respect to the domains of the production processes (e.g., involving metastable dissociative excitation or electron impact excitation or dissociative electron recombination of ions etc.,), in different discharge

media, and on the effects of the surrounding environment (e.g., N_2, O_2, and water vapor content) to understand the non-equilibrium nature of the plasmas. The production processes involved in exciting the molecule to a certain rotational state with N' numbers determine the occurrence of rotational–translational equilibrium. This means that detailed investigation of the elementary production mechanisms and the population of the generated rotational levels (in a certain N' domain of interest) in molecules under study is highly desirable before considering their population distribution as a measure of the T_{gas}.

Against a background of the above factors, a study simultaneously involving multiple molecular species (e.g., OH (A–X), NO-γ (A–X), and N_2 (C–B)) to determine T_{rot} and T_{vib} could prove to be imperative to provide a broader perspective to the awareness of the various production mechanisms and the rotational populations in certain ranges of N' numbers, especially in the case where argon is used as the plasma fill gas in a wet environment, because the presence of $Ar^*_{meta}(^3P_2)$ stable states governs the formation chemistries of a humid plasma discharge, which in turn produces numerous reactive nitrogen and oxygen species ((e.g., OH (A), N_2 (A), and SPS N_2 (C)). Concerning the derivation of the rotational and vibrational temperatures of the considered diatomic molecules, we are mainly interested in utilizing conventional spectroscopic-based diagnostics such as the Boltzmann plot and related software modules such as LIFBASE and SPECAIR. However, unlike a number of studies that have adopted double fittings models approach to fit the rotational level populations in the Boltzmann plot to estimate the OH (A–X) band T_{rot} (equivalent to T_{gas}) [12], [13], in the present work, only a single fitting model has been successfully adopted to fit the rotational structure of OH (A–X) in a wet discharge region. The Boltzmann plot with a single fitting has often been used to determine the T_{gas} in conventional gas discharges between metallic electrodes, nonetheless, adaptation of this model has resulted in higher T_{rot} of OH (A–X) for the plasma discharges in a humid environment [23].

The objective of this study is to characterize the atmospheric pressure AC-excited argon gas-liquid-phase discharge using spectroscopic diagnostic techniques. Moreover, the electrical properties of the discharge are analyzed by an electrical method; in addition, the discharge is evaluated visually by capturing high speed images. The formation mechanisms for the populated non-equilibrium rotational levels of various diatomic molecules are realized qualitatively by investigating the optical emission spectra.

The key contribution of the present work is the successful utilization of the single fitting Boltzmann plot model to derive the T_{rot} of OH (A–X) in a wet environment; moreover, discrepancies in the measured T_{rot} corresponding to the same discharge region are elaborated based on the excitation mechanisms (particularly those involving metastable states) and the N' numbers. Based on analysis of (1) the hydroxyl OH band due to the electronic transition from the upper state ($A\ ^2\Sigma^+$) to the ground state ($X\ ^2\Pi$), (2) the gamma-band system of nitric oxide NO-γ due to the electronic transition from the upper state ($A\ ^2\Sigma^+$) to the ground state ($X\ ^2\Pi$), and (3) the second positive system of nitrogen SPS N_2 due to the electronic transition from the upper state ($C\ ^3\Pi_u$) to the lower state ($B\ ^3\Pi_g$), the T_{rot} and the vibrational temperatures (T_{vib}) are determined from a single spatially resolved spectrum (in the spectral range 200 to 415 nm) being recorded in the corresponding region of the discharge in the gas- or liquid-phase. By employing different methodologies, fourteen distinct temperatures were measured and comparisons made for a discharge region in the gas-phase with that in the liquid-phase, that is, the Boltzmann plot T_{rot} of OH (A–X), LIFBASE T_{rot} and T_{vib} of OH (A–X), LIFBASE T_{rot} and T_{vib} of NO-γ (A–X), and SPECAIR T_{rot} and T_{vib} of N_2 (C–B). The production mechanisms and the rotational populations for the various diatomic molecules are thoroughly discussed to explain the causes of the variations in the T_{rot} in a humid discharge.

II. EXPERIMENTAL SETUP

A schematic sketch of the experimental device is exhibited in Figure 1 (a), and the optical configuration for experimentation is displayed in Figure 1 (b). The gas-liquid-phase (two-phase) discharge assembly comprises of a cylindrical stainless-steel (CSS) electrode (outer diameter 2.0 mm) kept in a coaxial manner inside a fused quartz tube with inner diameter of 5.5 mm. From the end view of the fused quartz tube, the CSS electrode is adjusted at a gap of 8.0 mm. The discharge assembly is installed in an acrylic glass chamber filled with deionized water (DIW). For generation of the two-phase plasma, argon gas (99.99% pure) is injected through the CSS electrode with a flow rate of 1.2 slpm, and then the discharge assembly is lowered below the surface ($D_- = 10$ mm) of DIW by adjusting a micrometer caliper. The gap spacing is 8.0 mm, which is the separation between the tip of CSS electrode and the DIW surface. Before conducting experiments, the chamber is filled each time with 400 ml of fresh DIW. A cooling setup is attached with the two-phase reactor

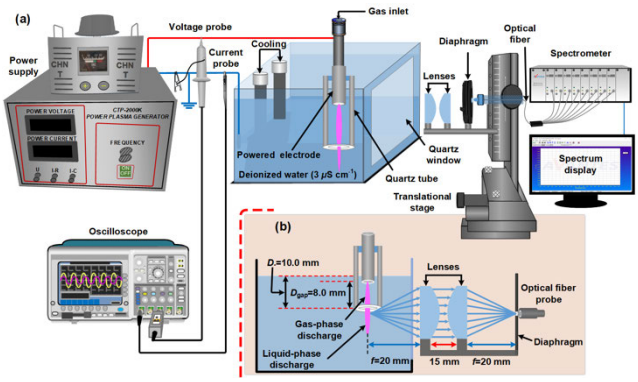

FIGURE 1. Schematic of the experimental setup (a), and the optical arrangement for spatially resolved measurements (b).

to control the temperature of the DIW at 25°C. The CSS electrode of the discharge assembly is connected with a high voltage AC power supply (Corona Lab CTP-2000K) with the driving frequency fixed at 22 kHz, and the DIW electrode is grounded. The voltage and current waveforms are recorded by an oscilloscope (Tektronix DPO4034) with a high-voltage probe (Tektronix P6015A) and a current probe (Tektronix TCP0030A), respectively. The visible light emission patterns of the discharge are recorded using a Canon camera (EOS7d). Spectroscopic measurements are performed with a multichannel spectrometer (Avantes Avaspec; grating 1800 grooves mm^{-1}). Spatially resolved emission spectra are obtained using the optical setup outlined in Figure 1(b). This optical arrangement for experimentation is analogous to the one adopted in a previous study concerned with measurement of the spatial emission profiles [17].

III. EXPERIMENTAL RESULTS AND DISCUSSION

A. DESCRIPTION OF THE DISCHARGE OPTICAL EMISSION PATTERNS

The discharge first started at the tip of the CSS electrode, and became localized just above the breakdown threshold ($V_{rms} = 2430$ V) for the plasma gas. When the $V_{rms,d}$ value was raised to a higher level, the discharge expanded suddenly and occupied the entire interelectrode spacing volume ($V_{rms,} = 2490$ V). It was noted that just after the breakdown, the $I_{rms,d}$ value of the discharge current was only 2 mA. When $V_{rms,d}$ was further increased from 2430 to 4700 V, the $I_{rms,d}$ increased from 2 to 20 mA. These values for the discharge current were much smaller than those occurring in conventional atmospheric plasmas excited between metallic electrodes [24], [25]. This is because current was flowing through the DIW electrode.

In the gas-phase (inside the quartz tube), the discharge formed in a stable constricted channel. Whereas, in the liquid-phase it evolved as a plume-like shape (PLS), as typically observed in a conventional plasma jet in the gas phase [26]. The question then arises as to whether the PLS structure sustained in the gas-phase (which results from the gaseous discharge flowing into the liquid-phase) or in the liquid-phase. In an attempt to enhance our understanding of these basic processes, typical images of the discharge, which are displayed in Figure 2, were analyzed. A computer code routine was used to measure the dimensions of the discharge in the liquid-phase (below the opening surface of the quartz tube). The hole generated as a consequence of gas flowing in the downstream direction was short in length (∼2 mm) relative to the length of the PLS (∼6 mm) in the liquid-phase (Figure 2(a)). Moreover, with an increase in the $V_{rms,d}$ value, the length of the PLS structure also increased in both the radial (from ∼2 mm to up to ∼4 mm) and the downstream directions (from ∼6 mm to up to ∼8 mm) (Figures 2(b) and (c)). In contrast, expansion of the conventional plasma jet plume in the gas phase typically occurs in the direction of the stream. Visually, it was also noticed that the structure of the PLS was not stable and it moved around at the onset value of the applied voltage, although, to some extent, it still retained the plume shape, as shown in Figure 2. A distinctive phenomenon of direct-liquid discharges is their unstable nature. Our experiments confirmed that such direct-liquid discharges were highly unstable and spread in a chaotic manner in the liquid-phase. Such discharges are also called streamer discharges [27]. Another interesting phenomenon was the reduction in length of the PLS, this being observed by recording an image of the discharge at 8 min after initiation. The property associated with the shortening of the length of the discharge is also a factual phenomenon observed for direct-liquid discharges whereby an escalation in liquid conductivity occurs [28]. Thus, in the present experiments, the evidence for shortening of the length of the PLS is consistent with the discharge existing in the liquid-phase. Based on these observations it can be concluded that the structure of the PLS was not that of a gas-phase discharge, rather it was a liquid-phase discharge might be consisting of multiple nonstationary streamers.

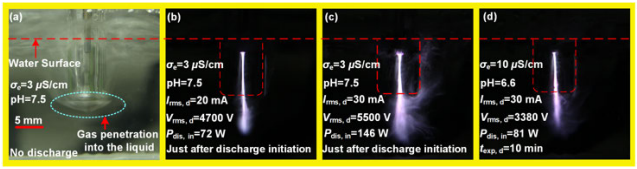

FIGURE 2. Image of the discharge assembly when the discharge is not excited (a), and images of the discharge as a function of operating time (b)–(d) recorded with a fixed camera shutter speed of $t_{shutter} = 100$ ms.

Here a short description is given to explain the breakdown mechanism for a discharge (PLS structure) in the liquid-phase. Historically, there were two schools of thought related to the formation of discharge in liquids. The first theory was based on the electron multiplication, and second theory was based on the bubble breakdown mechanism. In DIW, free electrons by and large are not present. Even if they are in DIW, they are immediately solvated (1 ps time scales) [27]. Thus, here electron avalanche phenomenon is less probable because of the utilization of high purity DIW (3 μs cm^{-1}). Moreover, powered electrode is located at a distance of 8.0 mm from the liquid surface. So, one may assume that electric field at the liquid surface should be weaker to boost the impact ionization, converting it into an electron avalanche, and then further triggering the multiplication of electron avalanches. Thus, the propagation of discharge in liquid most probably can be the result of micro-bubbles formation in the liquid-phase. According to bubble theory, formation of micro bubbles requires joule heating (provided by the high gas temperature of discharge at the liquid surface). These bubbles believed to serve as a source of local electrical breakdown which further begin the breakdown process and initiate the streamers.

The increase in length of the PLS with increase in the applied voltage from $V_{rms,d} = 4700$ V to $V_{rms,d} = 5500$ V (power increases from $P_{dis,in} = 72$ W to $P_{dis,in} = 146$ W), as shown in Figure 2, may be associated with increased

dissociation processes. This implies that the discharge is responsible for sustaining an increased dissociation of the plasma, consequently it gains length at higher applied voltages. In contrast, by keeping the discharge current constant, when the exposure time of the discharge is extended by up to 10 min, clearly results in a reduction in the length of the PLS. At the longer exposure time, the number of ions are increased as a result of the dissociation and ionization of water molecules. Furthermore, in the presence of air, gaseous acidic contamination products such as NO_2^- and NO_3^- species are produced. These species may be responsible for the increased electrical conductivity of the liquid (Figure 2), resulting in a shorter length of the PLS. At the edge of the discharge channel, an increasing σ_e weakens the electric field in the Maxwellian relaxation time and discontinue the further process of dissociation [29]. At this stage, extension of the discharge requires more energy to sustain the discharge in order to compensate for the reduction in the electric field near the channel edge. Nevertheless, it is evident that the discharge power, in this case, has decreased due to a drop in the discharge voltage after operation for 10 min. Thus, ultimately a reduction in the electric field is accompanied by a shortening of the PLS length.

B. VOLTAGE AND CURRENT WAVEFORM

The voltage and current waveforms corresponding to the discharge images in Figures 2(b) and 2(c) are presented in Figures 3(a) and 3(b), respectively. Just after initiation of the discharge, the recorded current waveform indicates a discharge current pulse (DCP) situated at rising edge of every half-period (Figure 3). According to the results, a decrease in the amplitude of the DCP is detected with increasing applied voltage, and a sinusoidal-like current waveform without a DCP is witnessed with the further increase in applied voltage, as shown in Figure 3(b). The current waveforms with the aforementioned characteristics were also reported and discussed in our previous studies [17], [30], where focus was given to the temporal evolution and variation in shapes of the waveforms (for description of the nature of the discharge). At that time, minimal consideration was given to explaining the underlying discharge mechanisms that control the emergence of the DCP.

Herein, an analysis is conducted on the current waveforms in an attempt to understand the reasons for the appearance and disappearance of the DCP under different discharge conditions. A characteristics time period (CTP) during which magnitude of the discharge current maintains at a certain minimum level whereby the corresponding discharge voltage rises continuously from zero to a certain value is observed initially for all the current waveforms, an example of which is displayed in Figure 3(a). Starting from the current waveform in Figure 3(a), the discharge current remains at a minimum for a time period of 5 μs. Afterwards, a rise in the discharge current is seen with further increase in the discharge voltage. For the case in Figure 3(b), the discharge current remains at a

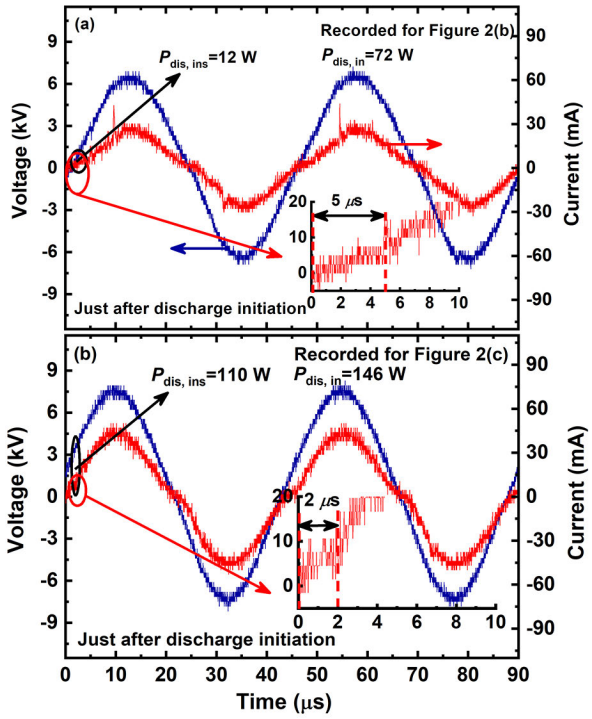

FIGURE 3. Typical current vs voltage waveforms of Figures 3(a) and 3(b) are recorded for the discharge images presented in Figures 2 (b) and 2 (c), respectively.

minimum with a continuously increasing discharge voltage in a similar manner to that observed for the case in Figure 3(a).

In contrast, in this case, the CTP is much shorter as the discharge current starts increasing after 2 μs. This is due to the fact that $P_{dis,in}$ is raised to 146 W, implying that more power is absorbed into the discharge compared to the case for 72 W in Figure 3(a). This clearly indicates that $P_{dis,in}$ is an important parameter that may reduce the CTP followed by the extinction of the DCP on the current waveform. To validate this assumption in Figure 3(a), the instantaneous power of the discharge ($P_{dis,ins}$) was measured within the CTP and compared with the $P_{dis,ins}$ for the case in Figure 3(b). It may be seen that $P_{dis,ins}$ within the CTP in Figure 3(a) is 14 W, a value which is much less than 110 W, as measured for the case in Figure 3(b). This shows that for the discharge of Figure 3(a), the conductivity is much weaker during the CTP, and continuously increasing the discharge voltage may trigger an electron avalanche (to sustain the discharge before it dies out), which abruptly elevates the discharge current. In Figure 3(b), in contrast, the conductivity of the discharge during the CTP is much higher, so a smoother current waveform is obtained. Therefore, it is clear that the discharge power during the CTP is crucial for the appearance and disappearance of the DCP on the current waveform. A relationship between the CTP and DCP can also be inferred from inspection of the current waveform, namely, that a larger CTP is followed by the DCP. For example, in the present case, a CTP of 5 μs results in the emergence of the DCP and no DCP

is observed on the current waveform for a relatively smaller CTP of 2 μs. Here the two-phase discharge in the reactor based on the appearance of DCP on the current waveform is considered to be in a streamer-like mode [10].

C. COMPARISON OF THE OPTICAL EMISSION SPECTRA OF THE DISCHARGE REGIONS IN THE GAS- AND LIQUID-PHASES

The two-phase discharge is further characterized by recording the spatially resolved emission spectra for two distinct locations in the discharge, that is, (1) in the gas-phase (1.0 mm from the tip of the CSS electrode) and (2) in the liquid-phase (4.0 mm from the inlet of the quartz tube), as illustrated in the inserts of Figure 4. The discharge region inside the quartz tube remains in the gas-phase due to the high flow rate (1.2 slpm) of the plasma gas, whereas the discharge region below the inlet to the quartz tube corresponds to the liquid-phase (wet environment). The purpose of recording spectra at these two distinct locations in the discharge is to identify the prevailing production mechanisms for the molecular species of interest. In the spectral range from 200 to 415 nm, the emission spectra for both locations are dominated by OH (A–X) and the SPS N_2 (C–B). In the spectral range from 650 to 815 nm, argon atomic lines are clearly dominant. In addition, the prominent atomic hydrogen Balmer alpha line (656 nm) and the atomic oxygen line (777 nm) are detected in both emission spectra. It is noted that the SPS N_2 (C–B) emission bands are more intense in the case of the spectra recorded in the gas-phase; in contrast, the OH (A–X) emission band is more intense in the liquid-phase (Figure 4). The important chemical reactions governing the discharge chemistries are described below.

The ·OH is one of the most active radicals with the highest oxidation potential, 2.85 V, and thus considered crucial in advanced oxidation processes. The emission intensity of OH (A–X) is much higher in the liquid-phase discharge region compared to that in the gas-phase, as revealed in Figure 4. Several possible reactions have been reported concerning the production of OH (A–X), and one of the important excitation mechanisms is the electron–impact dissociative excitation of a H_2O molecule:

$$\begin{aligned} &e^- + H_2O \rightarrow OH\,(A) + H + e^-, \\ &[k \approx 2 \times 10^{-19} - 1 \times 10^{-16}\ m^3s^{-1}, \\ &(T_e = (1 - 3\ eV)].\ [31] \end{aligned} \tag{R1}$$

A large amount of energy (12.6 eV) is required to ionize the water molecule, thus this reaction R1 would be feasible for directly yielding the ·OH production. Electron–impact dissociation of a water molecule proceeds to OH (X) via

$$\begin{aligned} &e^- + H_2O \rightarrow OH\,(X) + H + e^-, \\ &[k \approx 2 \times 10^{-18} - 9 \times 10^{-16}\ m^3s^{-1}, \\ &(T_e = (1 - 3eV)].\ [31] \end{aligned} \tag{R2}$$

The rate coefficients for the electron impact dissociation processes are calculated from the cross-sections

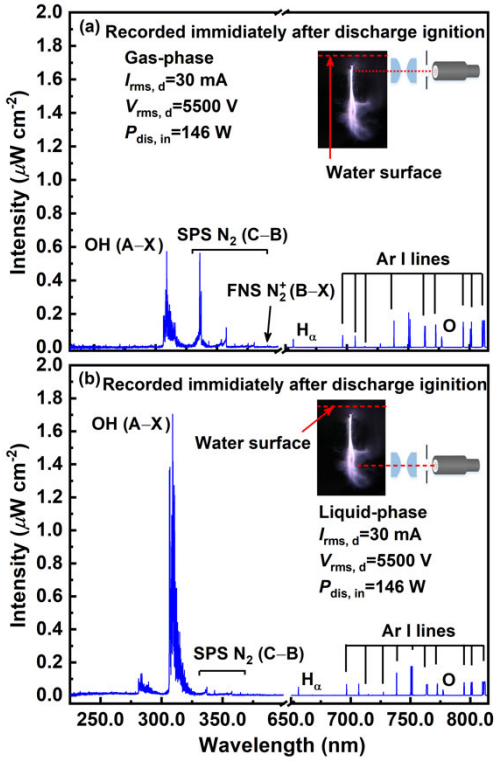

FIGURE 4. Overview of the spatially resolved emission spectra, collected for the discharge region in the gas-phase (a), and for the discharge region in the liquid-phase (b).

provided elsewhere [31]. Calculations are carried out based on the assumption that electron distribution is Maxwellian. The resultant OH (X) via electron–impact reaction [R2] in the plasma:

$$\begin{aligned} &e^- + OH(X) \rightarrow OH\,(A) + e^-, \\ &[k \approx 3 \times 10^{-14} - 8 \times 10^{-13}\ m^3s^{-1}, \\ &(T_e = (1 - 3\ eV)].\ [32] \end{aligned} \tag{R3}$$

Electron–ion recombination reactions have also been proposed as a possible route for OH (A) production:

$$\begin{aligned} &e^- + H_2O^+ \rightarrow OH\,(A/X) + H, \\ &[k \approx 5 \times 10^{-14} T_e^{-0.5}\ m^3s^{-1}],\ [33] \end{aligned} \tag{R4}$$

$$\begin{aligned} &e^- + H_3O^+ \rightarrow OH\,(A/X) + H_2, \\ &[k \approx 1 \times 10^{-13} T_e^{-0.5}\ m^3s^{-1}].\ [34] \end{aligned} \tag{R5}$$

Last but not least, a dissociative excitation reaction of H_2O with the Ar^*_{meta} ($^3P_2$) stable state is also crucial for the production of OH (A):

$$\begin{aligned} &Ar^*_{meta}(^3P_2) + H_2O \rightarrow OH\,(A) + H + Ar, \\ &[k \approx 8 \times 10^{-16}\ m^3s^{-1}, T_{gas} = 300\ K],\ [36],\ [37] \end{aligned} \tag{R6}$$

and is frequently proposed in several studies [35], [38], [39]. The $Ar^*_{meta}(^3P_2)$ stable state is resonant with the Rydberg levels of a water molecule, and thus, in a wet environment, reaction R6, in particular, seems critical for the formation of

OH (A). The emission bands for the SPS N_2 (C–B) transition are dominant for the discharge spectrum in the gas phase [Figure 4(a)]. Lower emission intensities for SPS N_2 (C–B) in the liquid-phase discharge spectrum may be the result of less exposure to air, as the spectrum is recorded well below from the water surface (D- = 14.0 mm). The SPS N_2 (C–B) can be generated from the highly localized electron–impact reactions with N_2 (X) or N_2 (A):

$$e^- + N_2(X) \rightarrow N_2(C) + e^-, \quad [k \approx 1 \times 10^{-19} - 3 \times 10^{-16}\ m^3s^{-1}, \quad (T_e = (1 - 3\ eV)], \quad [40] \tag{R7}$$

$$e^- + N_2(A) \rightarrow N_2(C) + e^-, \quad [k \approx 6 \times 10^{-16} - 3 \times 10^{-14}\ m^3s^{-1}, \quad (T_e = (1 - 3\ eV)]. \quad [40] \tag{R8}$$

Moreover, the contribution of the Pooling reaction may also be considered in major reactions to lead to the production of N_2 (C–B) via the N_2 (A) metastable states:

$$N_2(A) + N_2(A) \rightarrow N_2(C) + N_2(X), \quad [k \approx 2 \times 10^{-16}\ m^3s^{-1}]. \quad [41] \tag{R9}$$

According to a simulation-based study conducted on describing the chemical kinetics of humid argon discharges, the excitation to N_2 (A) state was suggested through the following reaction:

$$Ar^*_{meta}(^3P_2) + N_2(X) \rightarrow Ar + N_2(A), \quad [k \approx 2 \times 10^{-17}\ m^3s^{-1}]. \quad [42] \tag{R10}$$

Besides, the occurrence of the Ar^*_{meta} ($^3P_2$) states is most probably the origin of N_2 (C) through the Penning reaction with N_2 (X):

$$Ar^*_{meta}(^3P_2) + N_2(X) \rightarrow Ar + N_2(C), \quad [k \approx 4 \times 10^{-17}\ m^3s^{-1}]. \quad [43] \tag{R11}$$

The SPS N_2 (C–B) transitions are relatively much weaker for the liquid-phase discharge region, as shown in Figure 4(b). Also, the first negative system of nitrogen FNS $N_2^+(B\ ^2\Pi_u^+ - X\ ^2\Pi_g^+)$ in ambient atmospheric air discharges was not witnessed for the discharge in the wet region. In contrast, its presence was confirmed for the discharge region in the gas-phase. The required threshold energy to produce FNS N_2^+ (B–X) via a molecule in the N_2 (X) state is about 18.8 eV, a level which is less probable through electron-impact processes due to a shift in the electron energy distribution function (EEDF) to the lower energy region in a relatively higher humidity [44]. Apart from these, frequently proposed reaction pathways for the production of atomic O are

$$e^- + H_2O \rightarrow H_2 + O\cdot + e^-, \quad [35] \tag{R12}$$

$$e^- + O_2 \rightarrow 2O\cdot + e^-. \quad [45], \quad [46] \tag{R13}$$

In an argon discharge, atomic O· can also be produced from Ar^*_{meta} states through the following reaction:

$$Ar^*_{meta} + O_2 \rightarrow Ar + 2O\cdot \quad [k = 2 \times 10^{-16}\ m^3s^{-1}]. \quad [35] \tag{R14}$$

The discussion concerning the chemical reaction pathways indicates that the discharge chemistries operating in the gas and liquid discharge locations are different according to the relative humidity and the availability of contaminant impurities (e.g., N_2, O_2) arising due to diffusion from the ambient air. These impurities are responsible for the production of various atomic and molecular species (e.g., OH, N_2 (A), N_2 (C), O, and H) and hence there is a degree of versatility in the discharge chemistry of the plasma discharge depending on the measurement location in the discharge. In connection with the production of these species, the roles of Ar^*_{meta} and N_2 (A) metastable states are important through reactions R6, R9–R11, and R14.

D. SPECTROSCOPIC METHODS FOR DETERMINATION OF THE ROTATIONAL TEMPERATURE (T_{rot})

In the present work, the extracted T_{rot} from OH (A–X), NO-γ (A–X), and SPS N_2 (C–B) bands in a discharge region situated in the gas-phase are compared with region of the discharge in the liquid-phase. Disparate spectroscopic diagnostics methods (e.g., the Boltzmann plot, LIFBASE software, and SPECAIR software) are exploited for derivation of the T_{rot} from rotational structure of the considered diatomic molecules. The production processes for the discharge are predicted qualitatively by investigating the recorded spatially resolved emission spectra, and the fractional population histograms are calculated through the LIFBASE simulation. It is important to point out that the T_{rot} for the OH (A–X), NO-γ (A–X), and SPS N_2 (C–B) bands are measured simultaneously from a single spatially resolved emission spectrum (recorded in the spectral range of 200 to 415 nm according to the optical setup of Figure 1 (b)) recorded either for the discharge region in the gas- or the liquid-phase. The optical emission spectra are measured right after initiation of the two-phase discharge under the same conditions as mentioned in Figure 2(c). Two distinct discharge locations are selected for gathering of the respective optical emissions: (i) for the gas-phase at a location 1.0 mm apart from the CSS electrode tip, and (ii) for the liquid-phase at a location 4.0 mm away from the opening surface of the fused quartz tube. Note that for measurement of the liquid-phase, the recorded molecular spectrum for SPS N_2 (C–B) is weak, and evidence for NO-γ (A–X) is completely absent in both the gas- and liquid-phases discharge regions; therefore, in this experiment, argon as a feed gas is mixed with 0.5% nitrogen to facilitate the recording of prominent emission signals for the SPS N_2 (C–B) and NO-γ (A–X) bands.

The OH molecular structure in the spectral range 306–310 nm comprises mainly three branches [Q_1, R_2, and P_1]. In this work, the Q_1 branch is selected to construct the Boltzmann plot. The line details of the Q_1 branch are provided in the inset of Figure 5. There are various advantages to be gained by selecting the Q_1 branch, namely, (i) the band is situated in a relatively less dense region of the OH (A–X)

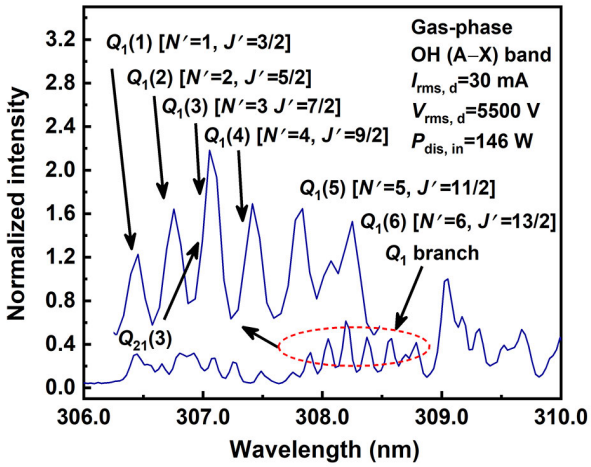

FIGURE 5. Identification of the Q_1 branch of the OH (A–X) emission spectrum collected for the discharge region in the gas-phase.

spectrum, so lines in this branch from $Q_1(1)$ to $Q_1(6)$ are well isolated; (ii) self-absorption of lines that appear in the wavelength range for this branch is not strong compared with the other lines except for $Q_1(3)$. Lines that undergo strong self-absorption result in a dip in the plot, and thus there is an alteration in the slope of the Boltzmann plot, which leads to an inaccurate estimation of the temperature. Therefore, the $Q_1(3)$ line that undergoes a strong self-absorption together with the neighboring line $Q_{21}(3)$ is eliminated from the Boltzmann plot calculation [23]; (iii) the lower rotational numbers of the Q_1 branch from ($N' = 1, J' = 3/2$) to ($N' = 6, J' = 13/2$), corresponding to lines $Q_1(1)$ to $Q_1(6)$, are feasible for minimizing the phenomenon of overpopulation. Thus, the Q_1 branch seems suitable for determining the $T_{\rm rot}$ from the OH (A–X) rotational-vibrational system ($A^2\sum^+, \upsilon' = 0 \rightarrow X^2\Pi_{3/2}, \upsilon'' = 0$). The distribution of intensities for the rotational population is given by the following formula [47]

$$I_{J'J''} = \frac{C_{\rm em}\sigma^4_{J'J''}}{Q_{\rm r}}(2J'+1)\exp\left(-\frac{B_\upsilon J'(J'+1)hc}{k_{\rm B}T_{\rm rot}}\right) \quad (1)$$

with factor $B_\upsilon J'(J'+1)$ the rotational energy $F(J')$, B_υ the rotational constant, h the Plank's constant, k_B the Boltzmann constant, $\sigma_{J'J''}$ the wavenumber for the rotational transition $J' \rightarrow J''$, $C_{\rm em}$ the emission coefficient, and $Q_{\rm r}$ the rotational partition function.

The LIFBASE software offers spectral simulation of various molecular bands including NO-γ (A–X), OH (A–X), CH (A–X), etc. [14]. This program is based on the most frequently used assumption attributed to the supposition that the rotational and vibrational levels populations are distributed in accord with the Boltzmann law. Using the LIFBASE software, the OH (A–X) spectral range from 306 to 310 nm is fitted according to the simulation. In the fitting process, $T_{\rm rot}$ is fixed at first to a certain value so that the smallest residual is compensated by varying the vibrational temperature ($T_{\rm vib}$) to obtain a best correspondence of the experimental spectrum with the calculated one. Note that the fitting process requires the measurement of a slit function (spectral line broadening due to instrumental broadening). In the gas temperature range from 300 to 6000 K, spectral lines broadening results primarily outcome in convolution of the optical emission spectrum, generating the slit function considered to be a Gaussian, with a full width at half maximum (FWHM). The slit function is determined by measuring the emission from a Hg lamp which emits a well-defined atomic line at 404 nm and is deemed to be almost a Gaussian distribution (FWHM = 0.0656 nm). The UV spectral range from 241 to 249 nm of the gamma-band system of NO was selected for analysis and compared with the calculated simulated spectrum. Besides, spectral simulation of the SPECAIR software also offers the facility of manipulating and fitting spectra [19]. Similar to the LIFBASE, SPECAIR also assumes that rotational populations of molecules in certain energy states are Boltzmann distributed. Unlike the LIFBASE, SPECAIR facilitates the spectral fitting of SPS N_2 (C–B). That is why, it is often used for approximation of the $T_{\rm rot}$ of SPS N_2 (C–B). In the present case, the SPS N_2 (C–B) bands at 353 and 357 nm were chosen for comparison with the simulated spectrum calculated by the SPECAIR.

E. ROTATIONAL TEMPERATURE ($T_{\rm rot}$) OF THE DISCHARGE IN THE GAS-PHASE REGION

The $T_{\rm rot}$ and $T_{\rm vib}$ values obtained from the gas- and liquid-phases of the discharge are provided in Table 1. In the gas-phase, the Boltzmann plot shows a good linear fitting (Figure 6), and thus, the acquired $T_{\rm rot}$ of 1078 ± 40 K has a good accuracy, and the $T_{\rm rot}$ can be assumed to equal the $T_{\rm gas}$.

TABLE 1. Derived $T_{\rm rot}$ and $T_{\rm vib}$ values for NO-γ (A–X), OH (A–X), and SPS N_2 (C–B) by the various spectroscopic methods.

NO.	Method	Band	$T_{\rm rot}$ (K)	$T_{\rm vib}$ (K)
1	Boltzmann plot	OH	1078±40	
	(gas-phase)	(A–X)	$T_{\rm rot}$=$T_{\rm gas}$	
2	LIFBASE	OH	1120±70	3600±210
	(Gas-phase)	(A–X)	$T_{\rm rot}$=$T_{\rm gas}$	
3	LIFBASE	NO-γ	1600±110	4000±240
	(Gas-phase)	(A–X)	$T_{\rm rot} > T_{\rm gas}$	
4	SPECAIR	N_2	1100±65	3500±200
	(Gas-phase)	(C–B)	$T_{\rm rot}$=$T_{\rm gas}$	
5	Boltzmann plot	OH	1474±80	
	(gas-phase)	(A–X)	$T_{\rm rot} > T_{\rm gas}$	
6	LIFBASE	OH	3400±170	5200±280
	(Gas-phase)	(A–X)	$T_{\rm rot} > T_{\rm gas}$	
7	LIFBASE	NO-γ	3900±180	5600±310
	(Gas-phase)	(A–X)	$T_{\rm rot} > T_{\rm gas}$	
8	SPECAIR	N_2	2700±130	5100±260
	(Gas-phase)	(C–B)	$T_{\rm rot} > T_{\rm gas}$	

The $T_{\rm rot}$ values for OH (A–X) and SPS N_2 (C–B) acquired using the LIFBASE and SPECAIR software are 1120 ± 70 K and 1100 ± 65 K, respectively. These methods generated fits

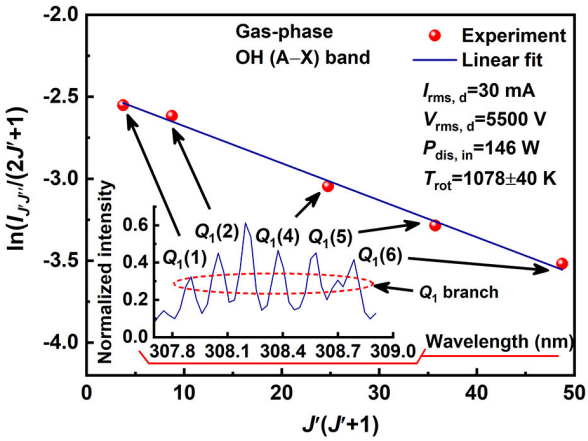

FIGURE 6. Boltzmann plot of the rotational population distribution (fitted with a single Boltzmann distribution) for the Q_1 branch of OH (A) as collected from the OH (A–X) emission spectrum recorded for a discharge region in the gas-phase.

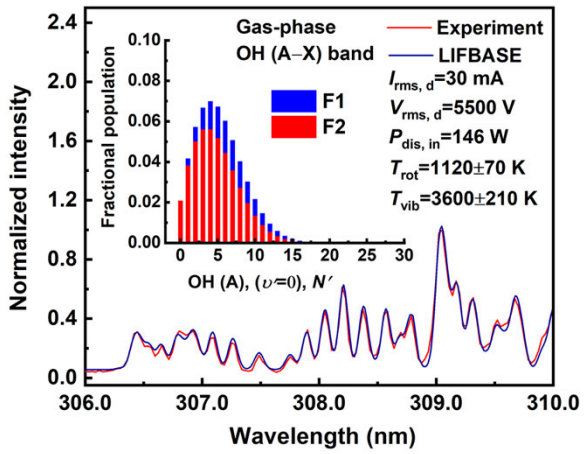

FIGURE 7. Fitting of the OH (A–X) emission spectrum by using the LIFBASE spectral simulation to measure T_{rot} and T_{vib}, for the case of a discharge region in the gas-phase. The fitting of the spectra is achieved by assuming a Boltzmann distribution for vibrational level (0–0). The insert displays the histogram for the fractional population calculated by the simulation.

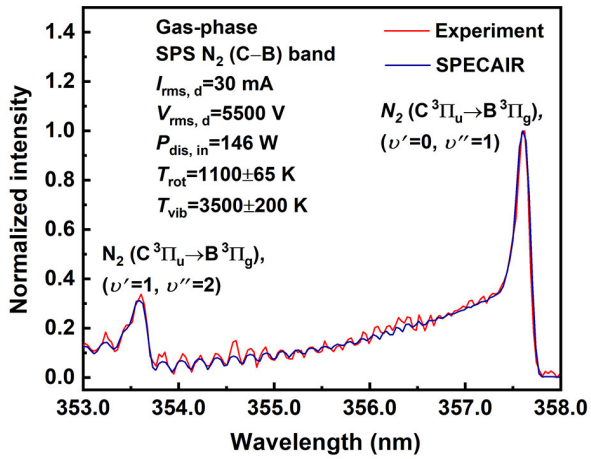

FIGURE 8. Fitting of the SPS N_2 (C–B) emission spectrum by using the SPECAIR calculation to measure T_{rot} and T_{vib}, for the case of a discharge region in the gas-phase. The fitting of the spectra is achieved by considering a Boltzmann distribution for vibrational levels (1–2) and (0–1).

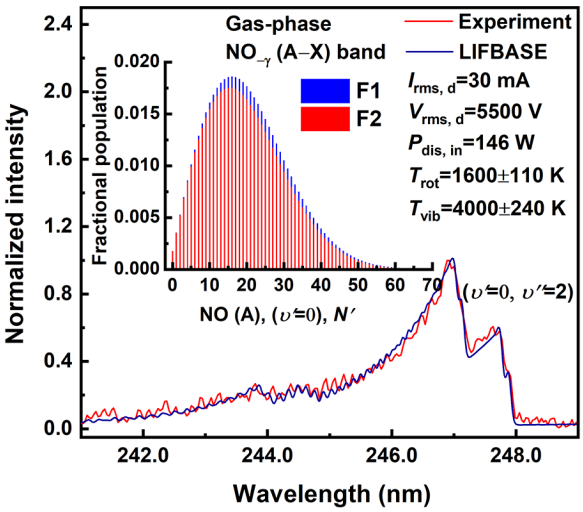

FIGURE 9. Fitting of the NO-γ (A–X) emission spectrum by using the LIFBASE spectral simulation to measure T_{rot} and T_{vib}, for the case of a discharge region in the gas-phase. The fitting of the spectra is achieved by considering a Boltzmann distribution for vibrational level (0–2). The insert shows the histogram of the fractional population calculated by the simulation.

which are concordant with the experimental measurements (Figures 7 and 8), suggesting the thermalized behavior for the rotational population distribution. Consequently, the predicted T_{rot} values can also be approximated as T_{gas} for the gas-phase. This is due to the fact that quenching collisions are less dominant with water molecules. That is, the translational-rotational energy exchange remains faster than the electronically excited state quenching. Under such conditions, the diatomic molecular rotational distribution is equilibrated with the translational distribution and the assumption of T_{rot} being equivalent to T_{gas} is validated.

For the case of NO-γ (A–X), the same fitting procedure is applied using LIFBASE. In spite of the fact that fitting of the spectra in Figure 9 is quite reasonable and thermalized distribution can be expected, it is known, however, that the obtained T_{rot} value is higher than the predicted temperatures based on using other methods applied to OH (A–X) and SPS N_2 (C–B), and thus, the T_{rot} manifestation for T_{gas} will overestimate the T_{gas} in the gas-phase. In this scenario, presumably thermalization is not achieved completely even though the fitting does indicate the Boltzmann distribution is realized. The fractional population histogram of NO-γ (A–X) calculated by the LIFBASE software predicts a maximum rotational population for $N' = 16$ (Figure 9), which means that the NO-γ (A–X) excited rotational levels are overpopulated for higher N' numbers. This phenomenon can be interpreted as an indication of there being residual

chemical energy through the production mechanisms of the molecules [16]. For these molecules at atmospheric pressure, electronically excited state quenching becomes faster than translational-rotational energy exchange, and thus, leads to a non-Boltzmann distribution. To elaborate further on this phenomenon, detailed discussion of the formation processes will be presented later in Section III (F).

F. ROTATIONAL TEMPERATURE (T_{rot}) OF THE DISCHARGE IN THE LIQUID-PHASE REGION

The T_{rot} value from the Boltzmann plot increases to 1474 ± 80 K for a discharge region in the liquid-phase, indicating non-Boltzmann behavior (Figure 10). Similarly, using the LIFBASE and SPECAIR methodologies, an increase in T_{rot} is also observed (Table 1). However, using the latter methods, a substantial increase in T_{rot} is witnessed. For example, when the LIFBASE method was applied to the NO-γ (A–X) spectrum recorded for a discharge region in the liquid-phase, the T_{rot} value obtained was 3900 ± 180 K.

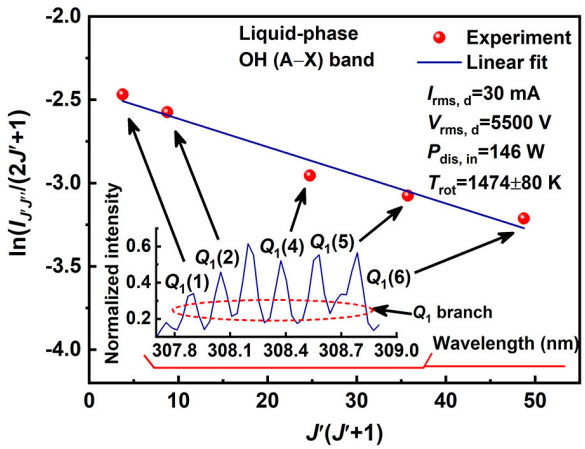

FIGURE 10. Boltzmann plots of the rotational population distribution (fitted with a single Boltzmann distribution) of the Q_1 branch of OH (A) as collected from the OH (A–X) emission spectrum recorded for a discharge region in the liquid-phase.

The T_{vib} values measured from the spectra of OH (A–X), NO-γ (A–X) and N_2 (C–B) are more than twice those of the corresponding T_{rot} values (Table 1). This may be explained by the way the vibrational energy transfer occurs, mostly as a consequence of electron collisions. The electron temperature (T_e) typically falls in the range 1–2 eV, which is a much higher temperature compared to that for a heavy particle.

The lower value of T_{rot} (1474 ± 80 K) is the consequence of using the Q_1 branch with low rotational numbers from ($N' = 1, J' = 3/2$) to ($N' = 6, J' = 13/2$). Though the estimated T_{rot} from selected rotational lines in the liquid-phase is still higher than the temperature of the discharge in the gas-phase, it is not related to the actual T_{gas}. This phenomenon is evaluated further by means of examples. In the first case, the $Q_1(6)$ line of the Q_1 branch is excluded, and thus, lines from Q_1 to Q_5 corresponding to the rotational numbers from ($N' = 1, J' = 3/2$) to ($N' = 5, J' = 11/2$) are employed for constructing the Boltzmann plot. Exclusion of the $Q_1(6)$ line from the calculation results in a noticeable drop in T_{rot} from 1474 ± 80 K to 1265 ± 50 K; nevertheless, T_{rot} is still higher compared to the gas discharge region [see Figure 11(a)]. Thus in the second case, only lines from $Q_1(1)$ to $Q_1(4)$ corresponding to the rotational numbers from ($N' = 1, J' = 3/2$) to ($N' = 4, J' = 9/2$) of the Q_1 branch, are accounted by constructing the Boltzmann plot [Figure 11(b)]. Using these lines, a linear fitting is quite reasonable, and the thermalized distribution is represented by a straight line, of which the slope is dependent on the T_{rot}. In this case the derived T_{rot} (1070 ± 35 K) is in good agreement with the T_{rot} value predicted by the Boltzmann plot in the gas-phase, and, in addition, also with those values inferred theoretically using the LIFBASE OH (A–X) and SPECAIR SPS N_2 (C–B) calculations as applied to the spectra of the discharge region in the gas-phase, as can be seen in Table 1.

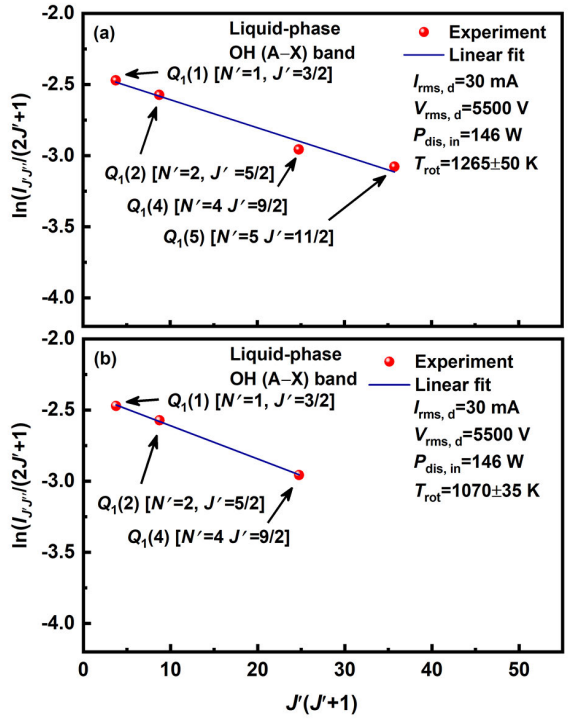

FIGURE 11. Boltzmann plots of the rotational population distribution of the Q_1 branch of OH (A) as collected from the OH (A–X) emission spectrum recorded for a discharge region in the liquid-phase; for the case with ($N' = 1, J' = 3/2$) to ($N' = 5, J' = 11/2$)presented in (a), and for the case with ($N' = 1, J' = 3/2$) to ($N' = 4, J' = 9/2$) presented in (b). The rotational distribution is fitted with a single Boltzmann distribution and the estimated T_{rot} values for the cases in (a) and (b) are 1265 ± 50 K and 1070 ± 35 K, respectively.

The transition probability of any given rotational structure is roughly proportional to the rotational number. With increasing rotational number the population term $\exp\left[-B_\upsilon J'(J'+1)hc/kT_{rot}\right]$ declines rapidly since the rotational energy $F(J')$ varies roughly as the square of the rotational number [48]. Therefore, moving along the optical branch with increasing rotational number, the intensity of the

lines is boosted at first, and acquires a maximum value, but thereafter the intensity decreases. This type of emission intensity distribution shows a good linear fitting, as also observed for the case of the Q_1 branch in Figure 6. However, the spectrum recorded for the discharge region in the liquid-phase reveals an increase in emission intensity at first with increasing rotational number and reaches a maximum at the $Q_1(3)$ line; nevertheless, the intensity starts to increase again after the $Q_1(4)$ line, unlike the emission intensity distribution of the Q_1 branch (Figures 6 and 10). This means for the case of the discharge spectrum in the liquid-phase with increasing rotational number, the aforementioned condition does not remain valid. Thus, the linear fittings carried out based on including the $Q_1(5)$ and $Q_1(6)$ lines will deviate from the Boltzmann distribution, as shown in Figures 10 and 11(a).

In a vapor bubble discharge at atmospheric pressure, the Boltzmann plot of OH (A–X) shows that the rotational states with a number larger than >10 clearly overpopulated [20]. Consequently, the rotational states with only lower numbers are thermalized. The Boltzmann plot constructed for the emission spectrum of OH (A) collected for a plasma jet in argon–water also has rotational population distributions acquired based on two linear fits; namely, the temperature from the rotational distribution with lower numbers ($N' < 13$) is 625 K, and the attained temperature for rotational distribution with higher numbers $13 < N' < 25$ is 5000 K [49]. A substantial difference between the T_{rot} is clear for rotational distributions having different N' numbers, and clearly the distribution belonging to higher N' numbers is not representative of T_{gas}.

It must be appreciated that the construction of Boltzmann plots in the aforementioned studies by employing two linear fittings to the rotational population distribution requires sophisticated spectrometers to record the spectra at high resolution. In contrast, a well-resolved Q_1 branch spectrum (utilized for Boltzmann fitting in our case) can be recorded even with a spectrometer with a grating of 1800 grooves/mm. More than that, using the Q_1 branch for construction of the Boltzmannn plot undoubtedly has technical merit in terms of ease of calculation by employing only a single fit to the population distribution. However, it is suggested that before applying the linear fit, the emission intensity distribution of lines from $Q_1(1)$ to $Q_1(6)$ of the Q_1 branch should be carefully examined, such that the line intensities in the branch are increasing at first and then decreasing, and later, the obtained fitting should also be inspected carefully to clarify whether the rotational distribution concurs with Boltzmann or not.

In a humid environment, fitting of NO-γ (A–X) and OH (A–X) using LIFBASE and fitting of SPS N_2 (C–B) using SPECAIR results in much higher calculated values of T_{rot} (Table 1). This means that non-Boltzmann behavior occurs for the higher rotational states of the employed bands. It is worth mentioning that the temperature parameter attributed to the overpopulation of the higher rotational states (for the cases of OH (A–X), NO-γ (A–X), and SPS N_2 (C–B)) falls in the range 2800 to 3900 K and this would seem to be independent of the nature of the discharge (such as glow or streamer type), the discharge current ($I_{\text{rms,d}} = 30$ mA), the pressure (ambient air), and the discharge feed gas (argon). This is considered a straightforward scenario whereby the rotational populations are a consequence of the formation processes, and thus, evaluation of the higher rotational populations can be performed by predicting possible production mechanisms based on analysis of the emission spectra of the discharge regions in the gaseous and wet environments.

In non-equilibrium plasmas, various essential reactions associated with OH (A) excitation are outlined in Section III (C). For the electron-impact excitation, a larger rate coefficient in comparison to the dissociative excitation of water suggests that direct excitation from OH (X) to OH (A) may be the governing reaction (reactions R1 and R3). Electron-ion recombination reactions (R4 and R5) may also produce overpopulation of higher rotational levels of OH (A). Apart from these processes, it has already been discussed in Section III (C) that Ar^*_{meta} ($^3P_2$) stable state and the Rydberg levels of the water molecule are resonant with each other [35], [38], [39], and thus, OH (A–X) production is stimulated in a wet environment via reaction R6. As shown in Figure 4, with the identical discharge conditions, the absolute intensity for OH (A–X) increases more than two orders of magnitude in the discharge region in the liquid-phase compared to the location in the gas-phase. This phenomenon confirms in a qualitative way the increased formation of OH (A–X) in a wet environment and also implies that the Ar^*_{meta} ($^3P_2$) stable state induce dissociative excitation of water molecules through R6 such that this pathway could be responsible for large excitations to higher rotational levels of the produced OH (A) state. These results imply that the OH (A–X) rotational levels population is populated via the formation process, and therefore, the deduced T_{rot} is overestimated because the rotational population distribution is non-Boltzmann. This hypothesis can be validated by the fractional population histogram that predicts the highest population for $N' = 8$, comparatively higher than $N' = 4$ as predicted for a gas-phase discharge spectrum of OH (A–X) (Figures 7 and 12). Due to this phenomenon, the fitted OH (A–X) spectrum (assuming the Boltzmann distribution using LIFBASE) for a discharge region in the liquid-phase yields a T_{rot} (3400 ± 170 K) much higher than T_{rot} (1120 ± 70 K) of a discharge region in the gas-phase.

The OH spectrum recorded for a pulsed discharges operated in helium or argon bubbles in tap water was compared with a reference spectrum calculated by using LIFBASE to obtain the T_{gas} [50]. It was shown that, the OH (A–X) rotational population is sensitive to the formation process, especially situating at higher numbers, and these are better to be characterized with a two-temperature fitting distribution. A discharge sustained between metallic and liquid electrodes characterized by conducting spatial measurements of the T_{rot} of OH (A–X) shown that, the deduced values of T_{rot} using LIFBASE are drastically higher near the liquid electrode region (reaches to 3100 K at the liquid surface) compared to

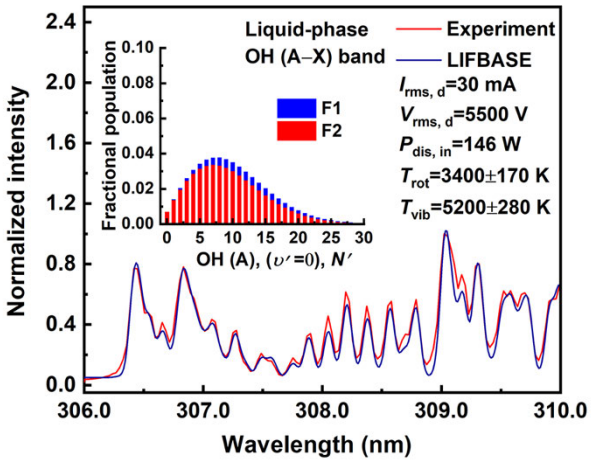

FIGURE 12. Fitting of the OH (A–X) emission spectrum by using the LIFBASE spectral simulation to measure T_{rot} and T_{vib}, for the case of a discharge region in the liquid-phase. The fitting of the spectra is achieved by assuming a Boltzmann distribution for vibrational level (0–0). The insert indicates the histogram of the fractional population calculated by the simulation.

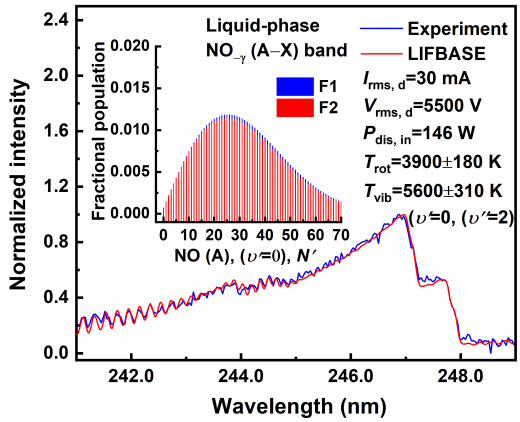

FIGURE 13. Fitting of the NO-γ (A–X) emission spectrum by using the LIFBASE spectral simulation to measure T_{rot} and T_{vib}, for the case of a discharge region in the liquid-phase. The fitting of the spectra is achieved by assuming a Boltzmann distribution for the vibrational level (0–2). The insert shows histogram of the fractional population calculated by the simulation.

a region near the metallic electrode (1050 K), and explicitly indicates the non-thermalization of the considered rotational levels population, populated by the formation process [17]. This means that, regardless of the spectroscopic technique employed, to represent the kinetic temperature, the rotational population (occurring at low or high N' numbers) must be thermalized for kinetic temperature representation.

In our previous work on an atmospheric discharge in argon sustained between liquid and metal electrodes using spatial measurements, it was shown that the absolute emission intensity of NO-γ (A–X) increases in a wet environment nearby region of the liquid electrode surface [17]. A similar case is observed in the present work, where an increased emission of NO-γ (A–X) is observed for the spectrum recorded (with argon as a feed gas mixed with 0.5% nitrogen) for a wet discharge region. In the case of argon as the plasma-forming gas, a reaction involving ·OH and N

$$\mathrm{N} + \cdot\mathrm{OH} \rightarrow \mathrm{NO}\cdot$$
$$[k \approx 4\exp\left(\frac{85}{T_g}\right) \times 10^{-17}\ \mathrm{m^3s^{-1}}].\ [35] \qquad \text{(R15)}$$

is commonly proposed for the formation of the NO· radical, especially in humid environments. As has been seen, generation of ·OH is efficient in humid environments and this clearly increases one of the reactants of R15. A study conducted to understand the chemistry of an atmospheric pressure plasma in argon using kinetic modeling shown that, N is exclusively generated from the Ar^*_{meta} ($^3P_2$) stable state [35], and consequently, R15 is promoted to increase the yielding of NO·. However, here to explain the overpopulation phenomenon, it is also important to take into account the possible excitation mechanisms where, for example, NO (A) generation is most often the result of direct excitation instead of involving dissociation processes. For a plasma in He-N_2 mixtures and for a plasma in N_2 or N_2–O_2 or N_2–NO mixtures, respectively, driven by a pulsed RF and by a high-voltage pulse, a reaction involving NO (X) and N_2 (A)

$$\mathrm{NO(X)} + \mathrm{N_2(A)} \rightarrow \mathrm{NO(A)} + \mathrm{N_2(X)},$$
$$[k \approx 7 \times 10^{-17} - 8 \times 10^{-17}\ \mathrm{m^3s^{-1}}].\ [51],\ [52] \qquad \text{(R16)}$$

was proposed as the dominant excitation mechanism for the production of the NO (A) excited state [51], [52]. In a N_2–O_2 discharge excited by means of a pulsed RF, the excitation mechanism to NO (A) with comparatively large excitation of higher rotational levels ($N' > 20$) was also attributed to R16 [53]. Large deviations were witnessed for the T_{rot} from the T_{gas}. As illustrated, the chemical generation of NO· is stimulated in a wet environment through R15, and, therefore, one of the reactants in R16 is increased. In a study on a humid argon discharge where the yielding of N_2 (A) by the Ar^*_{meta} ($^3P_2$) stable state reaction (R10) with N_2 (X) was proposed [35], the subsequent excitation mechanism R16 becomes crucial in the wet environment for the excitation of NO from the ground state (X) to the excited-state (A), and this thus leads to a rotational population of rotational levels which is overpopulated in the higher N' numbers. For the case of a discharge in a wet environment, the LIFBASE simulation predicts highest population for $N' = 25$ in comparison with $N' = 16$, as estimated for the gas-phase discharge spectrum (Figures 9 and 13). Thus, the predicted T_{rot} (3900 ± 180 K) of NO-γ (A–X) is perceptibly higher for a humid discharge compared to the T_{rot} (1600 ± 110 K) for a discharge in the gas-phase.

The T_{rot} of OH (A–X), NO-γ (A–X), N_2 (C–B), and O_2 (B–X) were compared for a discharge ignited between liquid electrodes (tap water) in air at atmospheric pressure were compared with their estimated T_{rot} of 2600 K, 3800 K, 2200 K, and 2200 K, respectively [22]. The T_{rot} of OH (A–X) and NO-γ (A–X) were substantially higher compared to other

molecular transitions in the humid discharge. The differences in the various T_{rot} are associated with a differences in the production mechanisms operating in the discharge, as well as with the decay processes of the excited states. If the results reported elsewhere [22] are compared with those found in the present study based on using argon as a fill gas mixed with 0.5% nitrogen, the reaction mechanisms involving the excitation to higher rotational levels of the monitored molecules should be different. This is because generation of OH (A–X), NO-γ (A–X), and N_2 (C–B) is critically influenced both directly and indirectly by the presence of the Ar^*_{meta} ($^3P_2$) stable states (via R6, R9–R11, R15, and R16), which are absent in the previously referenced study [22]. This is the reason why the results for the estimated T_{rot} [22] are different from those of the present study. For example, the attained value of T_{rot} from the N_2 (C–B) is much higher than the expected T_{gas}, while in [22] the estimated T_{rot} for N_2 (C–B) denotes the actual T_{gas}.

The SPS N_2 (C–B) is commonly used for estimating T_{rot} using SPECAIR, and a particular focus is the case of atmospheric discharges with air as the main plasma-forming gas [18]. Typically, intense emission of SPS N_2 (C–B) is witnessed in the spectra of an atmospheric DBD plasma generated for argon–water vapor mixtures [49]. Spatially resolved measurements performed on an argon discharge in a gas-liquid environment have shown increased emission of SPS N_2 (C–B) near the liquid surface [17]. A similar phenomenon was observed in the present experiments, where an increased emission of SPS N_2 (C–B) was repeatedly observed in the spectrum for the liquid discharge region while comparing the spectra (recorded with argon as a feed gas mixed with 0.5% nitrogen) for discharge locations in the gas-phase and liquid-phase environments.

A nitrogen discharge excited with pulsed RF in the pressure range 2.4 mTorr–1.5 Torr was investigated in an attempt to understand the production mechanism of N_2 (C) [54]. It was found that the formation of N_2 (C) was predominantly the consequence of N_2 (X) excitation [54]. In the afterglow region where there is a drop in the T_e, the Pooling reaction R9 involving N_2 (A) and N_2 (A) metastable states interaction becomes the dominant excitation mechanism. Another study conducted on a corona discharge has shown that the T_e quickly decreases as a result of higher pressure (atmospheric pressure), and the afterglow production mechanism of N_2 (C) is govern by the Pooling reaction (R9) [51]. For direct-liquid discharges excited with DC, N_2 (C) excitation was also considered the result of the Pooling reaction (R9) [20].

The predominant excitation of N_2 (C) via the Pooling reaction requires a N_2 (A) metastable state density much higher than that in the ground state N_2 (X), and in several cases, this condition might not be achieved. To investigate the influence of filling gases (such as Ar, N_2, N_2O, air, etc.) particularly focusing on the rotational distribution of OH (A–X), higher rotational excitation of N_2 (C) was also reported for discharges in bubbles in water and atmospheric glow discharges sustained with liquid electrodes [12]. In a N_2O discharge excited with DC, the measured T_{rot} (2400 ± 200 K) of N_2 (C–B) was substantially exceeded than those measured in Air (1850 ± 150 K) and N_2 (1850 ± 150 K) discharges [12]. The high value of T_{rot} was ascribed as the result of N_2 (C) excitation through the production mechanisms such as electron and ion (N_2O^+) recombination and excitation through electron dissociation in a N_2O discharge. The rotational temperatures as predicted from the SPS N_2 (C–B) (captured from an atmospheric pressure plasma jet) were 1000 K and 1500 K, respectively, for the case of pure argon and argon water (0.76%) mixtures [49]. The rise in the derived value of the T_{rot} was connected to the excitation of N_2 (X) through (reaction R11). In fact, the presence of the ($^3P_2$) state in the discharge leads to their interaction with other species (e.g., N_2, H_2O, O_2, etc.), thus, causing a large range of nitrogen and oxygen species. As regard to the excitation of N_2 (C), the Penning excitation of N_2 (X) via the stable state could be important. This is because this process is a near resonance and is often proposed for the production of the N_2 (C) state, especially, for the case of discharges involving argon or argon mixed with small fractions of nitrogen as plasma-forming gases. Also, the density of produced molecules in the N_2 (C) state indicates a certain distribution that relies on the electronic state of Ar^*_{meta} ($^3P_2$ or $^3P_0$).

Based on what has already been discussed, it seems likely that both reactions R9 and R11 are important with regard to the formation of N_2 (C). However, one should be aware that reaction R16 involving N_2 (A) metastable as reactant to excite NO (X) to NO (A) has been extensively proposed as a means to populate the rotational levels to higher numbers even greater than $N' > 20$ [53]. In the existing case, similar results are witnessed for the case of NO (A) whereby the highest population is perceived for $N' = 25$ (Figure 13). This implies that the density of the N_2 (A) metastable state is sufficient in the wet discharge region. Based on this and on the larger rate coefficient ($k \approx 2 \times 10^{-16}$ m^3s^{-1}) for the Pooling reaction (R9) compared to the Penning reaction (R11) ($k \approx 4 \times 10^{-17}$ m^3s^{-1}), it is suggested that the Pooling reaction is the mechanism that could potentially excite NO (A) to a much larger rotational excitation in the wet environment. Irrespective of the rate constants, an alternative explanation relates to the fact that the energies of the Ar^*_{meta} stable states for $^3P_2$and $^3P_0$ are 11.5 eV and 11.7 eV [55], respectively, while the threshold energy requirement for excitation of N_2 (X) to N_2 (C) is only 11.1 eV [56]. Comparing the respective energies, the excitation of N_2 (X) to N_2 (C) by Ar^*_{meta} ($^3P_2$) stable state may be proposed. However, generation of the N_2 (A) metastable species via Ar^*_{meta} ($^3P_2$) stable species could be more favorable through reactions R10 and R11 given that the species lies at 6.2 eV above the ground state [55]. N_2 (A) are the sole input species that result in the occurrence of the Pooling reaction, and thus, may boost the Pooling reaction R9 to produce the N_2 (C) state. In such a case as mentioned above, the rotational population is thus populated by the formation process that, by and large, excite the

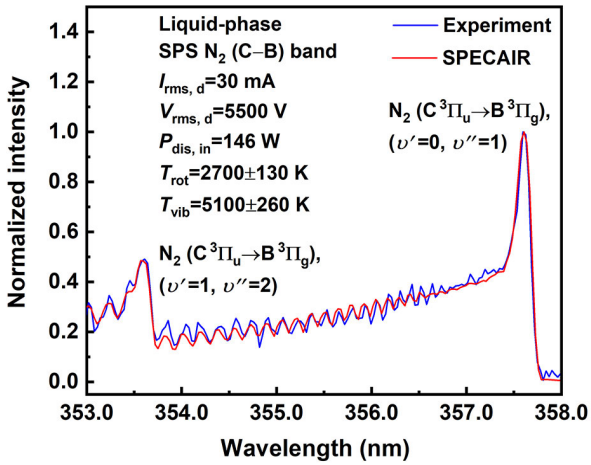

FIGURE 14. Fitting of the SPS N_2 (C–B) emission spectrum using the SPECAIR calculation to measure T_{rot} and T_{vib}, for the case of a discharge region in the liquid-phase. The fitting of the spectra is achieved by assuming a Boltzmann distribution for vibrational levels (1–2) and (0–1).

N_2 (C) to higher rotational levels, and as a result, the obtained populated rotational states are non-thermalized. This is the reason that the T_{rot} (2700 ± 130 K) predicted using the N_2 (C–B) is appreciably overestimated in the discharge region in the liquid-phase compared to the T_{rot} (1100 ± 65 K) for a discharge region in the gas-phase (Figures 8 and 14).

IV. CONCLUSION

This research has concerned studies on the experimental diagnostics of the argon gas-liquid-phase (two-phase) plasma discharge. From the recorded electrical signals, the pulses on the current waveforms were identified as the typical streamer-like behavior of the argon two-phase discharge. Image analysis indicated that discharge propagation through the liquid-phase (after the gas-phase discharge) depends on liquid properties and on discharge power input.

Several spectroscopic diagnostics techniques (e.g., Boltzmann plot, LIFBASE, and SPECAIR simulation methods) were used to extract the T_{rot} and T_{vib} from the simultaneously recorded OH (A–X), NO-γ (A–X), and SPS N_2 (C–B) diatomic molecular spectra either attained from discharge region in the gas- or in liquid-phase. The variations in temperatures in the gas- and liquid-phases of the discharge were inspected based on the metastable species and rotational quantum numbers. In the gas-phase, the T_{rot} measurements for the considered diatomic molecules were in good agreement, except for that estimated by NO-γ (A–X). Furthermore, the T_{rot} were found to be substantially higher in the humid environment for all the considered diatomic molecules.

In a humid environment, the calculated T_{rot} (1070 ± 35 K) via the Boltzmann plot and attained with a unique single fitting model (in comparison with that of a conventional two linear fittings models adopted for liquid discharges, as reported in the literature) only involving the rotational distribution of the lower rotational quantum numbers (from ($N' = 1, J' = 3/2$) to ($N' = 4, J' = 9/2$)) of the Q_1 branch of OH (A–X) provided a T_{rot} value that was found in excellent agreement with T_{gas} predicted by other methods (e.g., LIFBASE and SPECAIR simulation methods) in the gas-phase region. The overestimation of T_{rot} from various diatomic molecules come from the excitation of rotational population to higher N' numbers: for example this phenomenon was more pronounced for the case of NO (A) in the humid environment, where the maximum population occurred at $N' = 25$, resulted in the highest T_{rot} (3900 ± 180 K) compared to the estimated T_{rot} values for other molecular bands. This result provides evidence supporting the hypothesis of a strong T_{rot} dependence on the N' numbers. Accordingly, excitation to higher N' numbers was elucidated as the aftermath of the production processes, whereby the Boltzmann distribution for the considered rotational states was inhibited, and not related to the kinetic temperature. As for the totality of the production processes occurring in the aforementioned experiments in the argon discharge, these were Ar^*_{meta} ($^3P_2$) and N_2 (A) metastable based-processes that prevail practically exclusively in the liquid-phase region and favor the formation of various nitrogen and oxygen species (e.g., OH (A), NO (A), N_2 (A), and SPS N_2 (C)). This also gave support to the hypothesis proposed regarding the involvement of metastable species governing the chemistry of the argon discharge.

The Boltzmann method involving only a single fitting over the low numbers of the Q_1 branch of OH (A–X) has advantageous over the double Boltzmann plot model in a way that Q_1 branch rotational structure acquisition does not require sophisticated spectrometers compulsory for double fittings models to acquire highly resolved rotational structure. More than that, the attained fitting having the capability of detecting the deviation from the Boltzmann distribution compared to the simulation fitting methods (such as LIFBASE and SPECAIR). Besides, considering the case of simulation techniques, even with satisfactory fitting, and expecting them to be of the Boltzmann form by shape, the predicted T_{rot} values were significantly higher than the actual T_{gas}.

REFERENCES

[1] Z. Chen, S. Zhang, I. Levchenko, I. I. Beilis, and M. Keidar, "*In vitro* demonstration of cancer inhibiting properties from stratified self-organized plasma-liquid interface," *Sci. Rep.*, vol. 7, no. 1, p. 12163, Sep. 2017.

[2] Z. Xu, L. X. Wang, N. W. Zhang, and C. S. Hou, "Clinical application of plasma shock wave lithotripsy in treating impacted stones in the bile duct system," *World J. Gastroenterol.*, vol. 12, no. 1, pp. 130–133, Jan. 2006.

[3] K. Takaki, J. Takahata, S. Watanabe, N. Satta, O. Yamada, T. Fujio, and Y. Sasaki, "Improvements in plant growth rate using underwater discharge," in *Proc. J. Phys., Conf.*, Mar. 2013, vol. 418, no. 1, Art. no. 012140.

[4] E. Tatarova, N. Bundaleska, J. P. Sarrette, and C. M. Ferreira, "Plasmas for environmental issues: From hydrogen production to 2D materials assembly," *Plasma Sour. Sci. Technol.*, vol. 23, no. 6, Oct. 2014, Art. no. 063002.

[5] Q.-Y. Nie, H. I. A. Qazi, H.-P. Li, J.-Y. Chen, and C.-Y. Bao, "Degradation of organic compounds using a 2-D capillary discharge array in water," *IEEE Trans. Plasma Sci.*, vol. 42, no. 10, pp. 2628–2629, Oct. 2014.

[6] J. Yu, X. Zhang, Q. Lu, D. Sun, X. Wang, S. Zhu, Z. Zhang, and W. Yang, "Evaluation of analytical performance for the simultaneous detection of trace Cu, Co and Ni by using liquid cathode glow discharge-atomic emission spectrometry," *Spectrochim. Acta B, At. Spectrosc.*, vol. 145, pp. 64–70, Jul. 2018.

[7] D. Mariotti, J. Patel, V. Švrček, and P. Maguire, "Plasma-liquid interactions at atmospheric pressure for nanomaterials synthesis and surface engineering," *Plasma Processes Polym.*, vol. 9, nos. 11–12, pp. 1074–1085, Dec. 2012.

[8] I. Adamovich, S. D. Baalrud, and A. Bogaerts, "The 2017 plasma roadmap: Low temperature plasma science and technology," *J. Phys. D, Appl. Phys.*, vol. 50, no. 32, Aug. 2017, Art. no. 323001.

[9] M. R. Webb, F. J. Andrade, and G. M. Hieftje, "Use of electrolyte cathode glow discharge (ELCAD) for the analysis of complex mixtures," *J. Anal. At. Spectrometry*, vol. 22, no. 7, pp. 766–774, May 2007.

[10] J. Y. Park, P. V. Kostyuk, S. B. Han, J. S. Kim, C. N. Vu, and H. W. Lee, "Study on optical emission analysis of AC air–water discharges under He, Ar and N_2 environments," *J. Phys. D, Appl. Phys.*, vol. 39, no. 17, pp. 3805–3813, Aug. 2006.

[11] P. J. Bruggeman, N. Sadeghi, D. C. Schram, and V. Linss, "Gas temperature determination from rotational lines in non-equilibrium plasmas: A review," *Plasma Sources Sci. Technol.*, vol. 23, no. 2, Apr. 2014, Art. no. 023001.

[12] P. Bruggeman, D. C. Schram, M. G. Kong, and C. Leys, "Is the rotational temperature of OH (A–X) for discharges in and in contact with liquids a good diagnostic for determining the gas temperature?" *Plasma Processes Polym.*, vol. 6, no. 11, pp. 751–762, Nov. 2009.

[13] T. Verreycken, D. C. Schram, C. Leys, and P. Bruggeman, "Spectroscopic study of an atmospheric pressure dc glow discharge with a water electrode in atomic and molecular gases," *Plasma Sour. Sci. Technol.*, vol. 19, no. 4, Jun. 2010, Art. no. 045004.

[14] J. Luque and D. R. Crosley, "LIFBASE: Database and spectral simulation program (version 1.5)," SRI Int., Menlo Park, CA, USA, Tech. Rep. MP99-009, 1999.

[15] H. I. A. Qazi, M. Sharif, S. Hussain, M. A. Badar, and H. Afzal, "Spectroscopic study of a radio-frequency atmospheric pressure dielectric barrier discharge with anodic alumina as the dielectric," *Plasma Sci. Technol.*, vol. 15, no. 9, pp. 900–903, Sep. 2013.

[16] A. F. H. van Gessel, B. Hrycak, M. Jasiński, J. Mizeraczyk, J. J. A. M. van der Mullen, and P. J. Bruggeman, "Temperature and NO density measurements by LIF and OES on an atmospheric pressure plasma jet," *J. Phys. D, Appl. Phys.*, vol. 46, no. 9, Jan. 2013, Art. no. 095201.

[17] H. I. A. Qazi, M. A. Khan, and J. J. Huang, "Spatio-temporal evolution characteristics and pattern formation of a gas–liquid interfacial AC current argon discharge plasma with a deionized water electrode," *Plasma Sci. Technol.*, vol. 23, no. 2, Jan. 2021, Art. no. 025402.

[18] C. O. Laux, T. G. Spence, C. H. Kruger, and R. N. Zare, "Optical diagnostics of atmospheric pressure air plasmas," *Plasma Sour. Sci. Technol.*, vol. 12, no. 2, pp. 125–138, May 2003.

[19] C. O. Laux, "Radiation and nonequilibrium collisional-radiative models," in *Physico-Chemical Modeling of High Enthalpy and Plasma Flows*. Belgium, Rhode-Saint-Gense: Von Karman Institute, 2002.

[20] P. Bruggeman, D. Schram, M. Á. González, R. Rego, M. G. Kong, and C. Leys, "Characterization of a direct DC-excited discharge in water by optical emission spectroscopy," *Plasma Sour. Sci. Technol.*, vol. 18, no. 2, Mar. 2009, Art. no. 025017.

[21] H. I. A. Qazi, Q.-Y. Nie, H.-P. Li, X.-F. Zhang, and C.-Y. Bao, "Comparison of electrical and optical characteristics in gas-phase and gas-liquid phase discharges," *Phys. Plasmas*, vol. 22, no. 12, Dec. 2015, Art. no. 123512.

[22] P. Andre, Y. A. Barinov, G. Faure, and S. M. Shkol'nik, "Modelling radiation spectrum of a discharge with two liquid non-metallic (tap-water) electrodes in air at atmospheric pressure," *J. Phys. D, Appl. Phys.*, vol. 44, no. 37, Aug. 2011, Art. no. 375203.

[23] O. Motret, C. Hibert, S. Pellerin, and J. M. Pouvesle, "Rotational temperature measurements in atmospheric pulsed dielectric barrier discharge–gas temperature and molecular fraction effects," *J. Phys. D, Appl. Phys.*, vol. 33, no. 12, pp. 1493–1498, Jun. 2000.

[24] G. Li, H.-P. Li, W.-T. Sun, S. Wang, Z. Tian, and C.-Y. Bao, "Discharge features of radio-frequency, atmospheric-pressure cold plasmas under an intensified local electric field," *J. Phys. D, Appl. Phys.*, vol. 41, no. 20, Sep. 2008, Art. no. 202001.

[25] W.-T. Sun, G. Li, H.-P. Li, C.-Y. Bao, H.-B. Wang, S. Zeng, X. Gao, and H.-Y. Luo, "Characteristics of atmospheric-pressure, radio-frequency glow discharges operated with argon added ethanol," *J. Appl. Phys.*, vol. 101, no. 12, Jun. 2007, Art. no. 123302.

[26] D. Li, G. Li, J. Li, Z.-Q. Liu, X. Zhang, Y. Zhang, and H.-P. Li, "Promotion of wound healing of genetic diabetic mice treated by a cold atmospheric plasma jet," *IEEE Trans. Plasma Sci.*, vol. 47, no. 11, pp. 4848–4860, Nov. 2019.

[27] P. Bruggeman and C. Leys, "Non-thermal plasmas in and in contact with liquids," *J. Phys. D, Appl. Phys.*, vol. 42, no. 5, 2009, Art. no. 053001.

[28] K.-Y. Shih and B. R. Locke, "Optical and electrical diagnostics of the effects of conductivity on liquid phase electrical discharge," *IEEE Trans. Plasma Sci.*, vol. 39, no. 3, pp. 883–892, Mar. 2011.

[29] P. Šunka, "Pulse electrical discharges in water and their applications," *Phys. Plasmas*, vol. 8, no. 5, pp. 2587–2594, May 2001.

[30] H. I. A. Qazi, Y.-Y. Xin, H.-P. Li, M. A. Khan, L. Zhou, and C.-Y. Bao, "Effects of liquid electrical conductivity on the electrical and optical characteristics of an AC-excited argon gas–liquid-phase discharge," *IEEE Trans. Plasma Sci.*, vol. 46, no. 8, pp. 2856–2864, Aug. 2018.

[31] Y. Itikawa and N. Mason, "Cross sections for electron collisions with water molecules," *J. Phys. Chem. Reference Data*, vol. 34, no. 1, pp. 1–22, 2005.

[32] R. Riahi, P. Teulet, Z. Ben Lakhdar, and A. Gleizes, "Cross-section and rate coefficient calculation for electron impact excitation, ionisation and dissociation of H_2 and OH molecules," *Eur. Phys. J. D*, vol. 40, no. 2, pp. 223–230, Jul. 2006.

[33] D. M. Sonnenfroh, G. E. Caledonia, and J. Lurie, "Emission from OH(*A*) produced in the dissociative recombination of H_2O^+ with electrons," *J. Chem. Phys.*, vol. 98, no. 4, pp. 2872–2881, Feb. 1993.

[34] A. Neau, A. Al Khalili, S. Rosén, A. Le Padellec, A. M. Derkatch, W. Shi, L. Vikor, and M. Larsson, "Dissociative recombination of D_3O^+ and H_3O^+: Absolute cross sections and branching ratios," *J. Chem. Phys.*, vol. 113, no. 5, pp. 1762–1770, Aug. 2000.

[35] A. Schmidt-Bleker, J. Winter, A. Bösel, S. Reuter, and K.-D. Weltmann, "On the plasma chemistry of a cold atmospheric argon plasma jet with shielding gas device," *Plasma Sour. Sci. Technol.*, vol. 25, no. 1, 2015, Art. no. 015005.

[36] J. W. Sheldon and E. E. Muschlitz, Jr., "Quenching cross sections for $Ar(^3P_{0,2})$ and $Kr(^3P_{0,2})$ by H_2O and D_2O," *J. Chem. Phys.*, vol. 68, no. 11, pp. 5288–5289, Jun. 1978.

[37] S. Novicki and J. Krenos, "Absolute quenching cross section for collisions between $Ar(^3P_{0,2})$ and H_2O," *J. Chem. Phys.*, vol. 89, no. 11, pp. 7031–7033, Dec. 1988.

[38] J. B. Leblond, F. Collier, F. Hoffbeck, and P. Cottin, "Kinetic study of high-pressure Ar–H_2O mixtures excited by relativistic electrons," *J. Chem. Phys.*, vol. 74, no. 11, pp. 6242–6255, Jun. 1981.

[39] K. Tabayashi and K. Shobatake, "Dissociative excitation of water by metastable rare gas atoms: $Rg(^3P_{0,2})+H_2O \rightarrow Rg+OH(A\ ^2\Sigma^+)+H$ (Rg=Ar,Kr)," *J. Chem. Phys.*, vol. 88, no. 2, pp. 835–844, Jan. 1988.

[40] Y. Itikawa, "Cross sections for electron collisions with nitrogen molecules," *J. Phys. Chem. Reference Data*, vol. 35, no. 1, pp. 31–53, 2006.

[41] Y. Akishev, M. Grushin, V. Karalnik, A. Petryakov, and N. Trushkin, "On basic processes sustaining constricted glow discharge in longitudinal N_2 flow at atmospheric pressure," *J. Phys. D, Appl. Phys.*, vol. 43, no. 21, May 2010, Art. no. 215202.

[42] L. G. Piper, J. E. Velazco, and D. W. Setser, "Quenching cross sections for electronic energy transfer reactions between metastable argon atoms and noble gases and small molecules," *J. Chem. Phys.*, vol. 59, no. 6, pp. 3323–3340, Sep. 1973.

[43] N. Sadeghi, M. Cheaib, and D. W. Setser, "Comparison of the $Ar(^3P_2)$ and $Ar(^3P_0)$ reactions with chlorine and fluorine containing molecules: Propensity for ion–core conservation," *J. Chem. Phys.*, vol. 90, no. 1, pp. 219–231, Jan. 1989.

[44] L. Lin, Y. Lyu, B. Trink, J. Canady, and M. Keidar, "Cold atmospheric helium plasma jet in humid air environment," *J. Appl. Phys.*, vol. 125, no. 15, Apr. 2019, Art. no. 153301.

[45] M. A. Khan, J. Li, H. Li, and H. I. A. Qazi, "Characteristics of a radio-frequency cold atmospheric plasma jet produced with a hybrid cross-linear-field electrode configuration," *Plasma Sci. Technol.*, vol. 21, no. 5, May 2019, Art. no. 055401.

[46] M. A. Khan, J. Li, and H. Li, "Influences of the inner diameter of the solid shielding tube on the characteristics of the radio-frequency cold atmospheric plasma jet," *Plasma Sci. Technol.*, vol. 21, no. 9, Jul. 2019, Art. no. 095402.

[47] V. N. Ochkin, "Intensities in spectra and plasma energy distribution in the internal and translational degrees of freedom of atoms and molecules," in *Spectroscopy of Low Temperature Plasma*. Hoboken, NJ, USA: Wiley, 2009, pp. 147–233.

[48] A. G. Gaydon, "Measurements of effective temperature and studies with special sources," in *The Spectroscopy of Flames*. Dordrecht, The Netherlands: Springer, 1974, pp. 182–220.

[49] A. Sarani, A. Y. Nikiforov, and C. Leys, "Atmospheric pressure plasma jet in Ar and Ar/H_2O mixtures: Optical emission spectroscopy and temperature measurements," *Phys. Plasmas*, vol. 17, no. 6, Jun. 2010, Art. no. 063504.

[50] P. Bruggeman, F. Iza, P. Guns, D. Lauwers, M. G. Kong, Y. A. Gonzalvo, C. Leys, and D. C. Schram, "Electronic quenching of OH(A) by water in atmospheric pressure plasmas and its influence on the gas temperature determination by OH($A - X$) emission," *Plasma Sources Sci. Technol.*, vol. 19, no. 1, Dec. 2009, Art. no. 015016.

[51] M. Simek, V. Babický, M. Clupek, S. De Benedictis, G. Dilecce, and P. Sunka, "Excitation and decay of N_2 ($C\,^3\Pi_u$) and NO ($A\,^2\Sigma^+$) states in a pulsed positive corona discharge in N_2, N_2–O_2 and N_2–NO mixtures," *J. Phys. D, Appl. Phys.*, vol. 31, no. 19, pp. 2591–2602, Oct. 1998.

[52] N. K. Bibinov, A. A. Fateev, and K. Wiesemann, "On the influence of metastable reactions on rotational temperatures in dielectric barrier discharges in He-N_2 mixtures," *J. Phys. D, Appl. Phys.*, vol. 34, no. 12, pp. 1819–1826, Jun. 2001.

[53] S. De Benedictis, G. Dilecce, and M. Simek, "The NO ($A^2\Sigma^+$) excitation mechanism in a N_2-O_2 pulsed RF discharge," *J. Phys. D, Appl. Phys.*, vol. 30, no. 20, pp. 2887–2894, Oct. 1997.

[54] S. De Benedictis, G. Dilecce, and M. Simek, "Excitation and decay of N_2($B\,^3\Pi_g$,v) states in a pulsed discharge: Kinetics of electrons and long-lived species," *J. Chem. Phys.*, vol. 110, no. 6, pp. 2947–2962, Feb. 1999.

[55] S. Kanazawa, A. Ohno, T. Furuki, and K. Tachibana, "Temporal-spatial distribution of N_2 ($A^3\ \Sigma_u^+$) metastable molecules in the pulsed positive streamer in the needle-to-plate gap in sub-atmospheric pressure nitrogen," *J. Electrostatics*, vol. 103, Jan. 2020, Art. no. 103419.

[56] H. Nassar, S. Pellerin, K. Musiol, O. Martinie, N. Pellerin, and J. M. Cormier, "N_2^+/N_2 ratio and temperature measurements based on the first negative N_2^+ and second positive N_2 overlapped molecular emission spectra," *J. Phys. D, Appl. Phys.*, vol. 37, no. 14, pp. 1904–1916, Jun. 2004.

HAFIZ IMRAN AHMAD QAZI received the Ph.D. degree in plasma physics from the Department of Engineering Physics, Tsinghua University, Beijing, China, in 2018. He is currently a Postdoctoral Fellow with the College of Physics and Optoelectronic, Shenzhen University, Shenzhen, China. His current research interests include experimental studies and diagnosis on the atmospheric-pressure non-thermal plasmas and their applications, and plasma wall interaction.

JIAN-JUN HUANG graduated from the Department of Physics, Huaibei Normal College, Huaibei, China, in 1984. He received the Ph.D. degree from the Institute of Plasma Physics, Chinese Academy of Sciences, Hefei, China, in 2001. His current research interests include application of plasma physics and plasma wall interaction.